metals

MDPI

Article

Study on the Preparation and Corrosion Resistance Properties of Superhydrophobic Coatings on Galvanized Steel

Wenjuan Chen [1], Haoran Shi [1], Weiwen Liu [1], Anran Zhao [1], Gang Pan [2,*], Anding Huang [3], Yinglu Yu [1] and Luqi Ma [1]

[1] School of Materials Science and Engineering, Hefei University of Technology, Hefei 230009, China
[2] Department of Basic Course, Xuancheng Campus, Hefei University of Technology, Hefei 230009, China
[3] School of Chemistry and Materials Science, University of Science and Technology of China, Hefei 230009, China
* Correspondence: dagang@hfut.edu.cn

Abstract: The method of atmospheric corrosion protection of metals has always been a research hot spot at home and abroad. In this paper, superhydrophobic coating is prepared on the surface of galvanized steel by chemical etching using 1H,1H,2H,2H-perfluorodecyltriethoxysilane (PFDTES), graphene oxide (GO), anhydrous ethanol and water-based varnish as the main raw materials. The constitution of the superhydrophobic coating surface and the corrosion resistance of the steel are studied by electrochemical testing, X-ray diffraction (XRD), scanning electron microscopy (SEM), X-ray energy dispersive spectroscopy (EDS) and atomic force microscopy (AFM). Meanwhile, COMSOL software is used for the simulation of experiment. The results show that the surface of the superhydrophobic coating is composed of micro–nano sized papillary bulges, which play an important role in the improvement of metal corrosion resistance. The superhydrophobic coating effectively improves the alternating current impedance of the electrode and reduces the corrosion rate of the substrate. In addition, the results calculated by COMSOL software consist of the experimental results.

Keywords: 1H,1H,2H,2H-perfluorodecyltriethoxysilane; graphene oxide; superhydrophobic coating; corrosion resistance

Citation: Chen, W.; Shi, H.; Liu, W.; Zhao, A.; Pan, G.; Huang, A.; Yu, Y.; Ma, L. Study on the Preparation and Corrosion Resistance Properties of Superhydrophobic Coatings on Galvanized Steel. *Metals* **2023**, *13*, 260. https://doi.org/10.3390/met13020260

Academic Editor: Tomas Prosek

Received: 20 December 2022
Revised: 11 January 2023
Accepted: 25 January 2023
Published: 28 January 2023

1. Introduction

In order to improve the corrosion resistance of steel, the galvanization has been widely used in various fields, such as machine manufacturing, electronics, chemical industry, light industry, etc. [1–4]. When the zinc in the coating is corroded, oxides, zinc carbonate and other substances will be generated, which improves the compactness of the zinc film and isolates oxygen to prevent corrosion [5–9]. In order to further enhance the corrosion resistance of metals, researchers have made continuous efforts in exploring the optimization of metal corrosion prevention. In recent years, inspired by the surface structure of lotus leaves and other plants in nature, researchers have prepared superhydrophobic surfaces, of which the wetting angle is greater than 150° [10–12]. The superhydrophobic surface enhances the corrosion resistance due to its low surface energy, which can effectively reduce the contact area between metal and the corrosive. As it is difficult for droplets to stay, the superhydrophobic surface has a wide range of practical application value with the advantages of waterproof, anti-ice, anti-fog, and self-cleaning [13,14]. However, common preparation methods of the superhydrophobic surface have many disadvantages, such as tough and harsh conditions, cumbersome steps, and high cost. Furthermore, the superhydrophobic materials in use also have some problems of fragility, pollution-prone, etc. Thus, it will be a prevailing trend in the innovation of superhydrophobic preparation methods and the research on how to prolong the life of coating under harsh environments [15].

The metal will be hydrophilic due to its high surface energy. Therefore, the commonly used superhydrophobic modification method is using low surface energy materials to modify metal [16,17]. Fluorosilane is widely used as the superhydrophobic materials because of its low surface energy, heat-resisting, oil-resisting, oxidant-resisting and special physical and mechanical properties [18,19]. Wang et al. [20] used the sol-gel method to prepare the superhydrophobic surface. Li, Wang et al. [21] obtained fluorinated polyacrylate coating by electrospinning, and the wetting angle between the surface and water reached more than 150°. Li, Si et al. [22] obtained a superhydrophobic coating on the aluminum alloy surface by simple chemical etching and surface modification with 1H,1H,2H,2H-perfluoroalkyltriethoxysilane.

It is still a potential problem to improve the corrosion resistance of superhydrophobic coating. Graphene oxide (GO) is often used as a corrosion inhibitor for various metals because of its high specific surface area (about 300 m^2/g) and the electronegativity of oxygen-containing functional groups [23–26]. Ikhe et al. [27] used 1H,1H,2H,2H-perfluorooctyltriethoxysilane (PFOTES) to synthesize perfluoropolysiloxane (PPFS), and doped GO into the superhydrophobic coating to enhance the superhydrophobicity of surface for AZ31 magnesium alloy and prolong conduction of the corrosive, thereby improving the corrosion resistance of magnesium alloy finally. Compared with PFOTES, 1H,1H,2H,2H-perfluoroodecyltriethoxysilane (PFDTES) has lower surface energy and higher wettability due to the presence of fluorinated carbon [28]. It is a superhydrophobic agent that can be used to synthesize various functional coatings.

In this paper, the chemical etching method is adopted to form micron/nano-size rough surface using galvanized Q235B carbon steel as the base material. This study focuses on the influence of GO/PFDTES on the anti-corrosion properties of the superhydrophobic coating by means of XRD, SEM, AFM, electrochemical testing, and so on. In addition, the simulation by COMSOL software can prove the feasibility of the experiment and shorten the experimental cycle effectively.

2. Materials and Methods

2.1. Preparation of Test Specimens

The experimental material used in this work is Q235B low carbon steel (Anshan Iron and Steel Works, Anshan, China) [29], and its chemical composition (mass fraction, %): C 0.210, Si 0.210, Mn 0.580, S 0.036, P 0.017, Cu 0.020, Fe is the allowance. Precision wire cutting machine was used to cut several specifications of 10 mm × 10 mm × 5 mm Q235B steel specimens, which were drilled for electroplating easily. Six surfaces of each specimen were polished by sandpaper (MT, Guangzhou, China) of 220 #, 400 #, 1000 # and 2000 # in turn. The surfaces of the steel specimens were dried by a blower after grinding. The surfaces of steel specimens were electroplated by a zinc sheet (Chendu, China), and then the electroplated specimens were divided into three groups. The first group of electroplated specimens was without any treatment for comparative experiment (denoted by #1), the second group of electroplated specimens was varnished (denoted by #2), and the third group of electroplated specimens was varnished and superhydrophobic treated (denoted by #3).

2.2. Procedure of Varnishing and Superhydrophobic Treating

The hydrochloric acid, ethanol and sodium chloride were purchased from Sinopharm Inc., Beijing, China. The varnish was water-based epoxy varnish produced by Nippon Inc., Shanghai, China.

The electroplated specimens were etched with 1 wt% hydrochloric acid for 1 min, cleaned with deionized water, blew to dry, and varnished for standby.

10 mL of distilled water and 2 g of 1H,1H,2H,2H-perfluorodecyltriethoxysilane (PFDTES) (Dixin Chemical, Wuhan, China) were added into 100 mL of absolute ethanol, and then they were mixed by a LC-MSB-S magnetic stirrer (Lichen Inc., Hangzhou, China) at room temperature for one hour. The hydrophobic solution was obtained by means of adding 2 mL

of 2 mg/mL graphene oxide (GO) aqueous solution (Carbonfeng Technology Inc., Beijing, China) during the stirring process.

When the varnished specimens were completely dried, the surfaces of the specimens were coated with the superhydrophobic modifier. The coating was carried out again after the modifier was dried by airing, and the process was repeated three times. Finally, the specimens were dried for 8 h at room temperature to obtain a superhydrophobic coating. After taking a picture, the wetting angle can be directly measured on the picture, as shown in Figure 1.

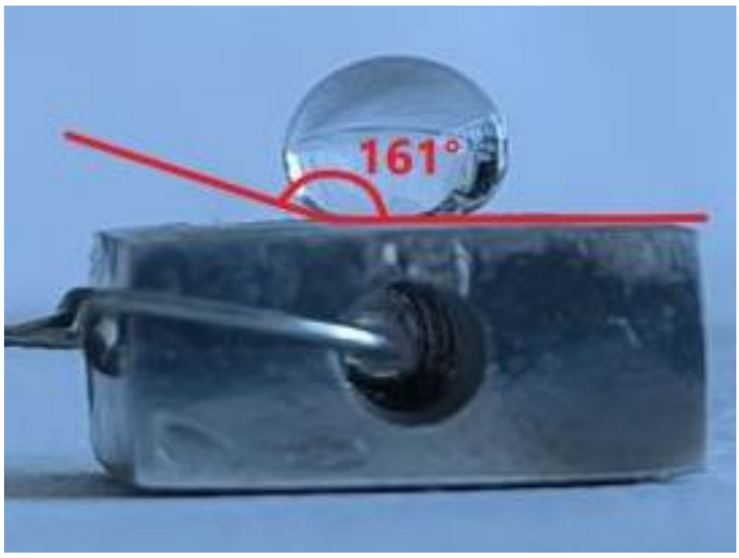

Figure 1. Superhydrophobic coating obtained in the experiment.

2.3. Corrosion and Performance Tests

The specimens #1~#3 were sealed with epoxy resin, which were exposed to only one surface to be tested, immersed in 3.0 wt% NaCl solution without degassing for 72 h, and then observed by various means.

The electrochemical impedance spectroscopy and potentiodynamic polarization curves of the specimens were measured using the CS310 electrochemical workstation (manufactured by Wuhan Ke Site in China). In the experiment, a three electrode system was used: the working electrode was the specimens with different corrosion time; the auxiliary electrode was a 4 cm^2 Pt sheet; the reference electrode was a saturated calomel electrode (SCE); the working temperature was room temperature (25 °C); all the potential values were relative to the potential of saturated calomel electrode; the electrolyte used in the experiment was 3.0 wt% NaCl solution; the frequency range of electrochemical impedance spectroscopy (EIS) was 10~100 kHz; the amplitude of disturbance AC potential applied during the test was 10 mV; the scanning potential range of the potentiodynamic polarization curve was ±0.3 V vs. Ecorr (relative to the self-corrosion potential); the scanning speed was 1 mV/s.

MR5000 metallographic microscope (Jiangnan Inc., Nanjing, China) was used to observe the surfaces of specimens and analyze surface corrosion.

DX-2700B X-ray diffractometer (XRD) produced by Malvern Panalytical in Shanghai, China was used to test the surface of specimens with different corrosion time and analyze the phase composition. The scanning speed of diffraction measurement was 2°/min. The phase composition was semi-quantitatively analyzed by comparing the relative peak strength of each phase in the XRD results.

Regulus 8100 scanning electron microscope (SEM) and energy dispersive spectroscopy (EDS) produced by Hitachi Inc. in Tokyo, Japan were used to characterize the surface of the specimens before/after corrosion and observe the surface morphology of the specimens.

Dimension Icon atomic force microscope (AFM) produced by Bruker Inc. in Karlsruhe, Germany was used to test the surface of specimens, analyze three-dimensional topography, and measure roughness of the surface.

2.4. Multi Physical Field Simulation

In order to further analyze the corrosion mechanism of the specimen surface, COMSOL software 5.6 (COMSOL Inc., Shanghai, China) [30,31] was used to conduct multi-physical field simulation through "secondary current distribution", "deformation geometry", "transport of diluted species" and "level set". The simulated model was established by imitating the seawater corrosion environment: the dimension of the two-dimensional profile model is 2×10^{-4} m wide, 2×10^{-4} m high, and the ambient temperature is 20 °C. The corrosion model of specimen #1 was simulated by directly exposing the electroplated specimens to seawater. The corrosion model of specimen #2/#3 contained three layers: the upper layer was seawater, the middle layer was varnish/superhydrophobic structure, and the lowest layer was zinc coating. In addition, in order to ensure the reliability of the simulation, the respective metallographic pictures of specimens #1~#3 were imported into the software for modeling. In addition, the main boundary conditions of COMSOL finite element simulation were shown in Table 1.

Table 1. The main boundary conditions of COMSOL finite element simulation.

Physics	**Boundary Condition**		
Secondary Current Distribution	Electrolyte	sigma	5 [S/m]
	Initial values	Electrolyte potential	0 [V]
		Electric potential	0 [V]
	Electrode surface	External electric potential	0 [V]
		Equation	Current density initialization
		Film resistance	No
		Dissolving-depositing species	Zn
		Electrode kinetics	Local current density expression
Deformed Geometry	Frame settings	Geometry shape function	1
	Free deformation settings	Mesh smoothing type	Hyperelastic
Transport of Diluted Species	Transport properties	Mobility	Nernst-Einstein relation
	Initial values	Concentration of Fe^{2+}	0
		Concentration of OH^-	1×10^{-4} [mol/m^3]
	Electrode surface coupling	Equation	Current distribution initialization
		Coupled reaction	Local current density
Level Set	Level set model	Equation	Current distribution initialization
	Initial values	Level set variable	Specify phase
Multiphysics	Nondeforming Boundary	Coupled interfaces	Secondary current distribution
		Boundary condition	Zero normal displacement
	Deforming Electrode Surface	Coupled interfaces	Secondary current distribution
		Moving boundary smoothing	Enable moving boundary smoothing
Definitions	Interpolation	Polarization curve	From experimental measurement
	Image	Import data model	From metallographic microscope picture

3. Results

3.1. Electrochemical Measurement

Figure 2 shows the results of AC impedance spectra of specimens after different corrosion time. As shown in Figure 2a, the high-frequency impedance modulus of specimen #1 is close to about 30 $\Omega \cdot cm^2$, while the low-frequency impedance modulus of 0.01 HZ gradually increases from 85.6 $\Omega \cdot cm^2$ to 701 $\Omega \cdot cm^2$ with the extension of corrosion time. In addition, the phase angle-frequency curves of specimen #1 (Figure 2a′) gradually shift to left with the extension of corrosion time, which may be related to the increasing corrosion products generated on the specimen surface. As shown in Figure 2b, the high-frequency impedance modulus of specimen #2 decreases from 588 $\Omega \cdot cm^2$ to 100 $\Omega \cdot cm^2$ with the extension of corrosion time, while the low-frequency impedance modulus of 0.01 HZ decreases from 6610 $\Omega \cdot cm^2$ to 1110 $\Omega \cdot cm^2$ with the prolongation of corrosion time. In addition, the phase angle-frequency curves of specimens #2 (Figure 2b′) gradually shift to the right with the extension of corrosion time, which may be related to the continuous penetration of water molecules. This shows that the corrosion resistance of varnish to metal substrate decreases rapidly with the prolongation of corrosion time. As shown in Figure 2c, the high-frequency impedance modulus of specimen #3 is close to about 150 $\Omega \cdot cm^2$, while the low- frequency impedance modulus of 0.01 HZ decreases from 3.14×10^9 $\Omega \cdot cm^2$ to 5110 $\Omega \cdot cm^2$ with the prolongation of corrosion time. In addition, the phase angle-frequency curves of specimen #3 (Figure 2c′) shifted to right with the extension of corrosion time, which may be related to the continual increase of water molecules infiltrated into the superhydrophobic coating on the specimen surface, and the constant damage of the surface coating. At the same time, by comparing Figure 2a–c, it can be seen that the low-frequency modulus of specimen #3 at each corrosion time is much greater than that of specimen #1 and specimen #2, which further indicates that corrosion resistance of the specimen can be more effectively enhanced by superhydrophobic modification through GO/PFDTES.

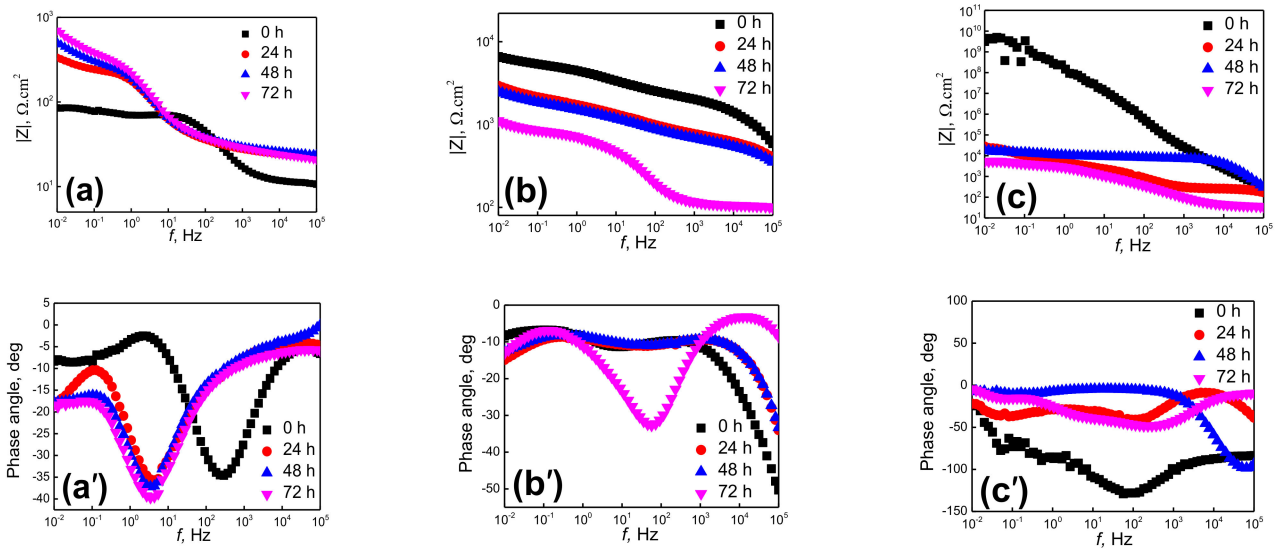

Figure 2. Bode plots of the EIS results for the rusted Q235B steel specimens at different corrosion times: (**a**,**a′**) for the specimens #1; (**b**,**b′**) for the specimens #2; (**c**,**c′**) for the specimens #3.

Figure 3 shows the polarization curves of specimens #1~#3 after different corrosion times. The polarization curves can effectively measure the corrosion rate of the specimen surface. The smaller the self corrosion current density is, the smaller the corrosion rate is; the more positive the self corrosion potential is, the smaller the corrosion tendency is. It can be seen from Figure 3a that the self-corrosion potential of specimens #1 gradually decreases from −0.43 V (SCE) to −1.08 V (SCE) with the prolongation of corrosion time, which may be related to the continual corrosion of the specimen surface. Figure 3b shows

that the self-corrosion potential of specimens #2 gradually decreases from −0.32 V (SCE) to −0.99 V (SCE) with the extension of corrosion time, which may be related to the continuous penetration of water molecules. Moreover, Figure 3c shows that the self-corrosion potential of specimen #3 gradually decreases from −0.15 V (SCE) to −0.97 V (SCE) and then increases with the prolongation of corrosion time, which may be due to the continuous penetration of water molecules and mutual fusion between particles in the coating.

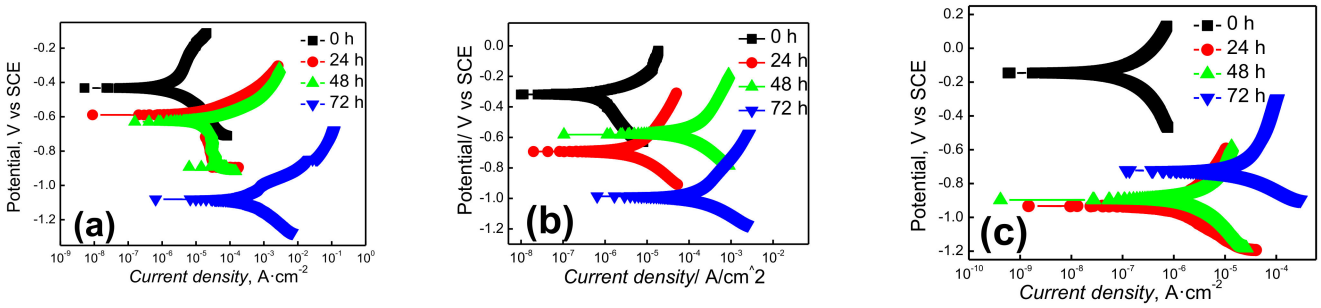

Figure 3. Polarization curves of electrodes at different corrosion time: (**a**) for specimens #1; (**b**) for specimens #2; (**c**) for specimens #3.

By fitting the polarization curves in Figure 3, the curves of self-corrosion current density are shown in Figure 4. It can be seen that the self-corrosion current density of specimen #1 increases from 2.55×10^{-6} A/cm^2 to 4.14×10^{-4} A/cm^2 with the extension of corrosion time, indicating that its corrosion resistance is relatively poor. The reason is that the zinc coating is quickly corroded in the corrosion solution, and then exposed to the steel substrate, resulting in a rapid increase in the corrosion rate. The self-corrosion current density of specimen #2 increases rapidly with the extension of corrosion time, and is finally similar to specimen #1, which indicates that the corrosion resistance of the varnish coating on the metal substrate is improved. The self-corrosion current density of specimen #3 does not change significantly with the extension of corrosion time. By comparing the three curves, it can be seen that the self-corrosion current density of specimen #1 is close to that of specimen #2 but far greater than that of specimen #3, which indicates that the superhydrophobic coating exerts a significant enhancement effect on the corrosion resistance of the metal substrate surface. The variation trend of impedance modulus with corrosion time in Figure 2 is some inconsistencies with the polarization curve, one of the important reasons may be that the polarization curve and impedance spectrum are tested with different specimens.

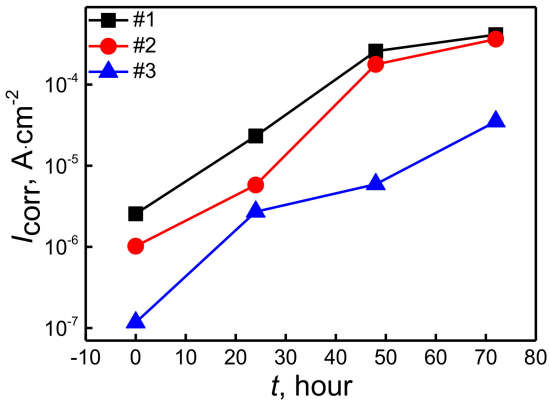

Figure 4. Corrosion current density of electrodes at different corrosion times.

3.2. Surface Morphology and Composition

As shown in Figure 5, the specimen surfaces before and after corrosion were photographed with a metallographic microscope. Figure 5a shows the surface photo of specimen #1 before corrosion. The surface is flat and smooth with scratches in the same direction, which is caused by sandpaper polishing. Figure 5a′ shows the surface photo of specimen #1 after 72 h corrosion. It can be seen that the zinc coating on the specimen surface has fallen off in a large area, causing corrosion and rust on the steel substrate of the inner layer. As shown in Figure 5b, the surface photo of specimen #2 before corrosion illustrates that most areas of the surface are flat, but there are a few small holes in some places. Figure 5b′ shows the surface photo of specimen #2 after 72 h corrosion, and several obvious corrosion bumps appear on the surface. The surface photo of specimen #3 before corrosion in Figure 5c shows that the surface is rough and there are some bumps, which are caused by the superhydrophobic coating on the specimen surface. The photo of specimen #3 after 72 h corrosion, as shown in Figure 5c, illustrates that the surface has not significantly changed before and after corrosion, and only few areas suffers the localized corrosion which may be caused by the penetration of water molecules.

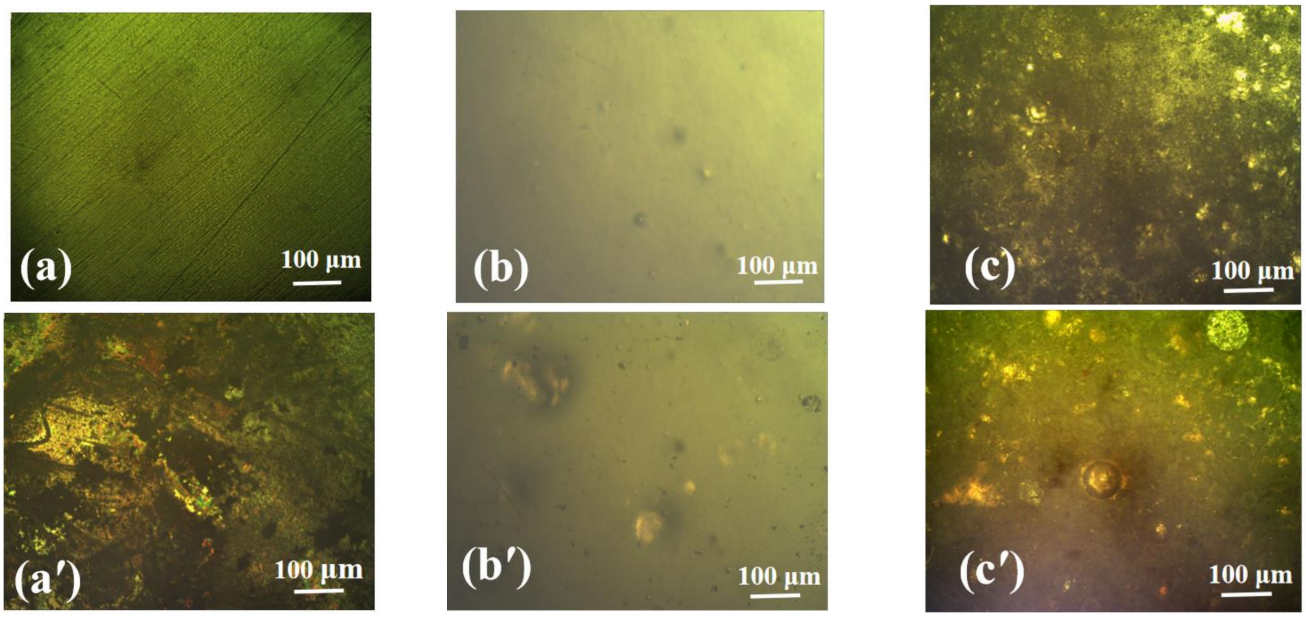

Figure 5. Metallographic images in different corrosion condition: (**a**,**a′**) for specimen #1 before/after corrosion; (**b**,**b′**) for specimen #2 before/after corrosion; (**c**,**c′**) for specimen #3 before/after corrosion.

Figure 6 shows the X-ray diffraction results of specimens #1~#3 before and after corrosion. As shown in Figure 6a, the surfaces of specimens #1~#3 before corrosion are mainly composed of Fe and Zn. The diffraction peak of Zn in specimen #1 is obviously higher than that of Fe, indicating that specimen #1 surface is mainly Zn coating. It is also found that the Zn diffraction peaks of specimens #2 and #3 are obviously weaker than that of specimen #1. The reason is that the varnish coating and superhydrophobic coating have a certain thickness, which leads to the weakening of X-ray diffraction intensity. In addition, it can be seen that the diffraction peaks of Fe and Zn are shifted, which may be related to the residual stress and crystal defects in the material [32]. As shown in Figure 6b, the surface of specimen #1 after 72 h corrosion is mainly composed of Fe, α-FeOOH, Fe_3O_4 and a small amount of Zn, which indicates that the Zn coating of specimen #1 is almost completely corroded during the immersion process, and the exposed steel substrate is corroded to form rust, which is attached to the specimen surface. The surface of specimen #2 after 72 h corrosion is mainly composed of Fe, α- FeOOH, Zn and a small amount of Fe_3O_4. Compared with specimen #1, the relative intensity of Fe in specimen

#2 decreases, while the relative intensity of Zn increases, which indicates that the varnish coating specimen has some corrosion resistance. However, the diffraction peak of specimen #3 shown in Figure 6b after 72 h corrosion has no obvious change compared to that before corrosion shown in Figure 6a. It can be inferred that the superhydrophobic coating has strong corrosion resistance capability, which can insulate the entry of corrosive media and protect the steel substrate from corrosion.

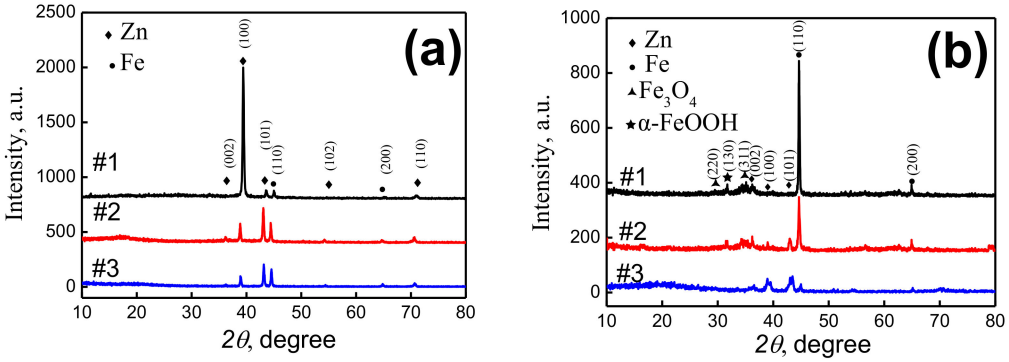

Figure 6. X-ray diffraction patterns of specimens #1~#3: (**a**) for specimens before corrosion; (**b**) for specimens after 72 h corrosion.

Figure 7 shows the SEM images of specimens #1~#3 before and after corrosion. According to Figure 7a, the surface of specimen #1 before corrosion is mainly composed of spherical particles, which is generally flat but multi-cracked. After 72 h corrosion, as shown in Figure 7a′, many holes and irregular branches appear in the surface, and some areas fall off, indicating that the zinc coating on specimen #1 is seriously eroded during the corrosion process. It can be seen from Figure 7b that the surface of specimen #2 is flat and dense before corrosion. After 72 h corrosion, as shown in Figure 7b′, many spherical particles appear on the surface, which may be related to the penetration of water molecules in the coating. According to Figure 7c, the observation of specimen #3 before corrosion shows that the coarse particles are stacked on the specimen surface in a form of spherical protrusions. After 72 h corrosion, as shown in Figure 7c′, it is found that the appearance of particles on the surface of specimen #3 is similar to Figure 7c, which reflects the excellent corrosion resistance of the superhydrophobic coating.

Figure 8 shows the EDS results (tested at 20 kV) of specimens #1~#3 before and after corrosion. The compositions presented were obtained under the assumption of material homogeneity and are given only to obtain qualitative information about the change in the composition of near-surface layers as a result of corrosion. Figure 8a,a′ shows the EDS spectra of specimen #1 before and after corrosion, respectively. It is seen that Zn mainly present in the spectrum before corrosion, with a small amount of Fe, O, and C. After 72 h corrosion the spectrum mainly contains Fe and O, with only a small amount of Zn left. This indicates that the zinc coating is continuously damaged during the corrosion process, and the steel substrate is exposed and then corroded. Figure 8b,b′ shows the EDS spectra of specimen #2 before and after corrosion, respectively. It can be seen that the spectrum before corrosion is mainly composed of C, with a small amount of Fe, O, Zn and other elements. After 72 h of corrosion, the spectrum is dominated by Zn, C and O, and the content of Fe element is also increased compared with that before corrosion, which indicates that the varnish coating is damaged after corrosion, and the zinc coating is exposed and then evidently corroded. For specimen #3, as shown in Figure 8c,c′, the spectra mainly contain C and F, with a small amount of Fe, Zn, O and other elements no matter before or after corrosion, which indicates that there is no obvious corrosion product on the surface of specimen #3 after 72 h corrosion. The results are consistent with that of XRD and demonstrate that the superhydrophobic coating has good performance in corrosion resistance.

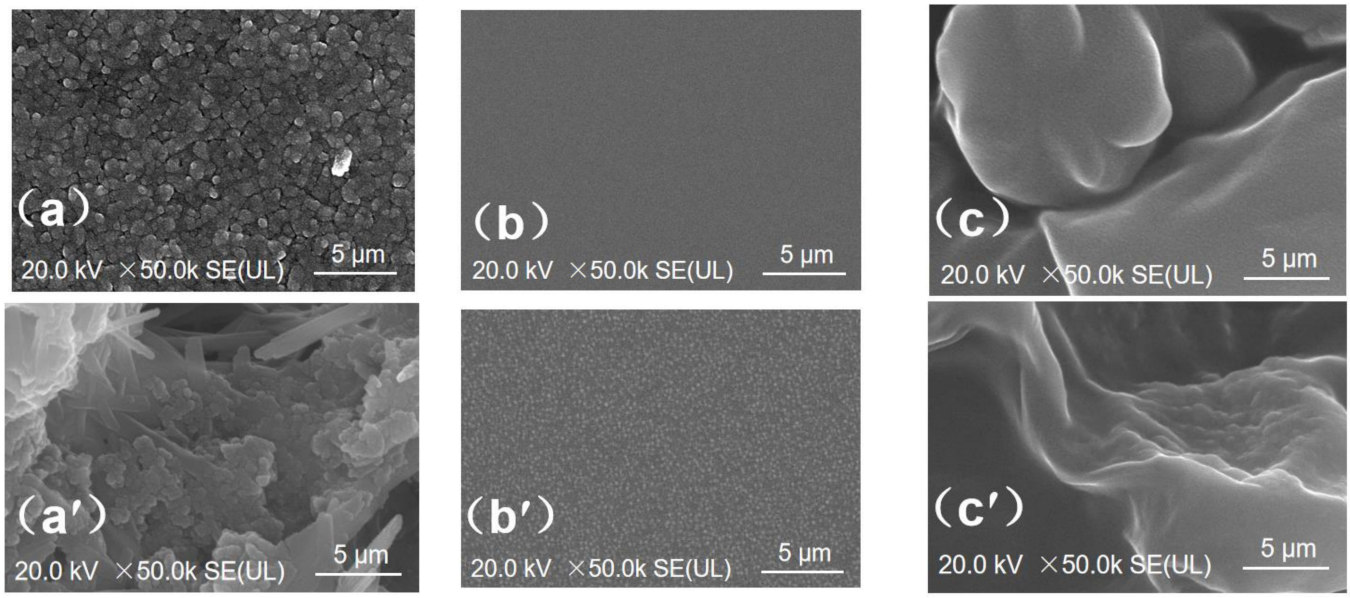

Figure 7. SEM images of specimen surface: (**a**,**a′**) for specimen #1 before/after corrosion; (**b**,**b′**) for specimen #2 before/after corrosion; (**c**,**c′**) for specimen #3 before/after corrosion.

The SEM results can only reflect the surface structure of specimens #1~#3 before and after corrosion, and the three-dimensional structure needs further analysis, so as to more comprehensively analyze the relationship between surface morphology and corrosion characteristics. Atomic force microscope (AFM) scanning was carried out to obtain the three-dimensional structure diagrams of specimens #1~#3 before and after corrosion, as shown in Figure 9. The surface roughness *R*a is obtained through the analysis of Nanoscope Analysis software, as shown in Table 2. It was found from Figure 9a that before corrosion, the grains of the zinc coating on the surface of specimen #1 are small and the size is basically the same, with a fluctuation range of −28.2 nm~31.3 nm. The surface roughness *R*a is 6.44 nm, which indicates that the surface of specimen #1 before corrosion is relatively flat and smooth. Figure 9a′ shows that there are large pits and bulges on the surface of specimen #1 after 72 h corrosion, with a fluctuation range of −913.5 nm~1.0μm. The surface roughness *R*a is 217 nm, which indicates that a large number of corrosion products are formatted after 72 h corrosion. It can be seen from Figure 9b that the surface of specimen #2 before corrosion is relatively flat with a fluctuation range of −21.3 nm~27.1 nm, and the surface roughness *R*a is 3.81 nm. Figure 9b′ shows that, after 72 h corrosion, the surface of specimen #2 has large pits and bulges with a fluctuation range of −290.7 nm~337.5 nm, and the surface roughness *R*a is 70.7 nm, which indicates that a certain amount of corrosion products is produced. It can be seen from Figure 9c that the bulges of specimen #3 are papillary with a fluctuation range of −52.6 nm~54.3 nm, which is similar to the lotus leaf structure, indicating that the superhydrophobic coating on the surface of specimen #3 is successfully coated. In addition, the surface roughness *R*a of specimen #3 before corrosion is 10.7 nm, and greater than that of specimens #1 and #2, which maybe due to the papillary bulges. It can be seen from Figure 9c′ that the three-dimensional image of the surface of specimen #3 after 72 h corrosion is similar to that before corrosion. Its surface roughness *R*a is 40.2 nm, which increases slightly compared with that before corrosion. This indicates that the appearance of surface before and after corrosion has little change, and there is no obvious accumulation of corrosion products. In addition, by comparing Figure 9a′–c′, it can be seen that after 72 h of immersion in 3.0 wt% NaCl solution, the surface of specimen #1 is corroded most seriously, followed by specimen #2, while specimen #3 has no obvious change, indicating that the corrosion resistance of the specimen after superhydrophobic treatment has been greatly improved.

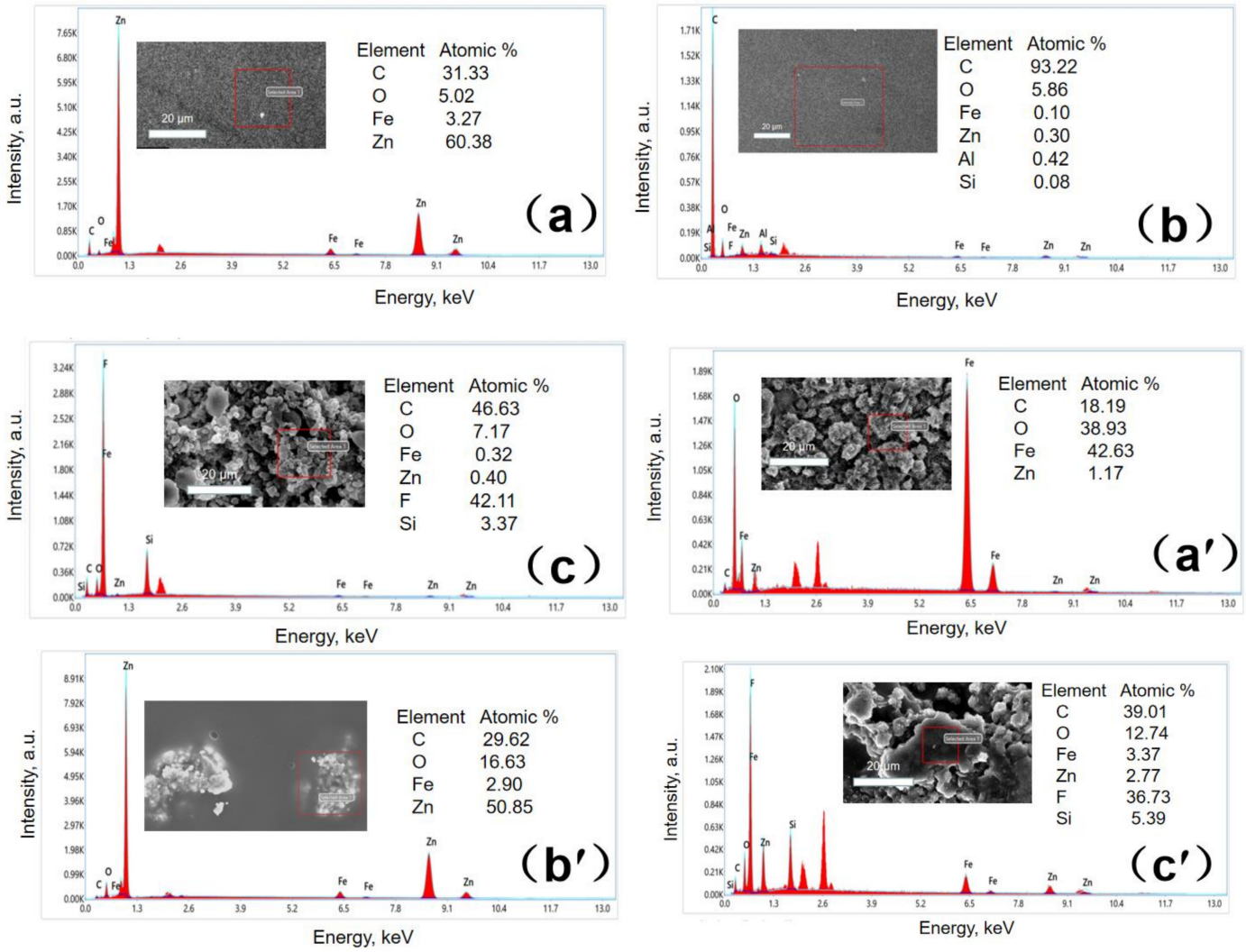

Figure 8. EDS line scanning spectrum of specimens: (**a**,**a′**) for specimen #1 before/after corrosion; (**b**,**b′**) for specimen #2 before/after corrosion; (**c**,**c′**) for specimen #3 before/after corrosion.

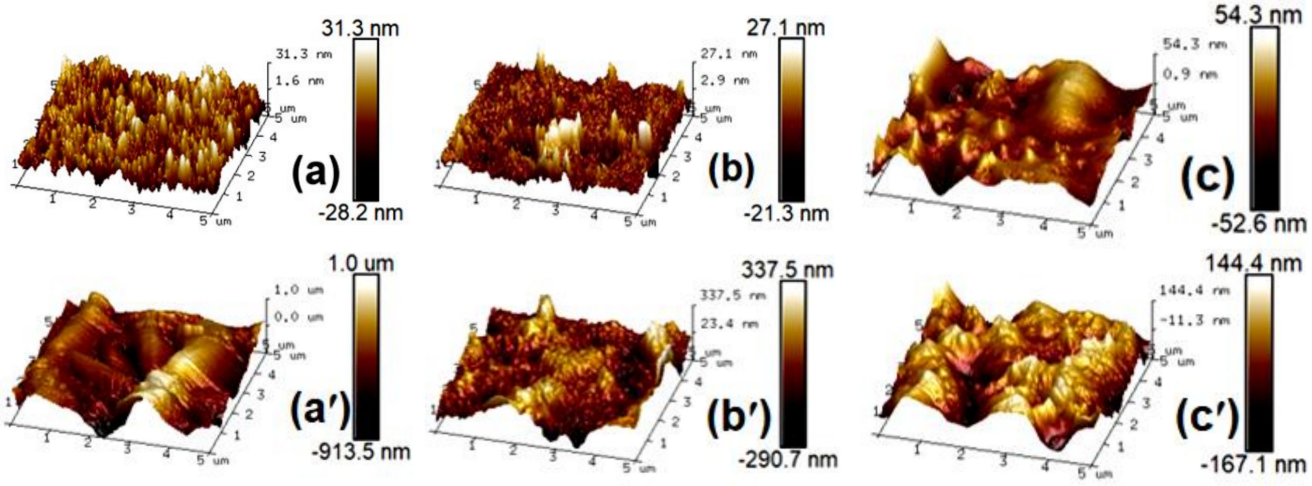

Figure 9. AFM three-dimensional structure of specimens surface: (**a**,**a′**) for specimen #1 before/after corrosion; (**b**,**b′**) for specimen #2 before/after corrosion; (**c**,**c′**) for specimen #3 before/after corrosion.

Table 2. The roughness *Ra* of specimens #1~#3 surface before and after corrosion.

Specimens	*Ra*/nm before Corrosion	*Ra*/nm after 72 h Corrosion
#1	6.44	217
#2	3.81	70.7
#3	10.7	40.2

4. Discussion

Based on the above experimental results, it can be seen that, compared with specimens #1 and #2, specimen #3 has the best corrosion resistance, which may be related to the papillary bulges formed on the surface. Then, the corrosion protection mechanism of superhydrophobic coating is further discussed through COMSOL finite element simulation results. Figure 10 shows the corrosion simulation results of specimens #1~#3. Figure 10a,c,e is the function pictures obtained after the metallographic photos of specimens #1~#3 before corrosion are imported into COMSOL software, respectively. Figure 10b,d,f are obtained by corrosion simulation on the surface defined by three function pictures. Figure 10b shows the simulation results of specimen #1 after 72 h corrosion. The white bulge in the corrosion area indicates the accumulation of corrosion products. The thicker the corrosion products, the more serious the corrosion. It can be seen that the entire surface of specimen #1 has obvious corrosion. Figure 10d shows the simulation results of specimen #2 after 72 h corrosion. It can be seen that the corrosion on the surface is also obvious, but the corrosion is relatively uniform relative to specimen #1. Figure 10f shows the simulation results of specimen #3 after 72 h corrosion. It can be seen that the corrosion of the surface is not obvious compared with specimens #1 and #2, indicating that the papillary bulges formed on the specimen surface after superhydrophobic treatment can significantly improve its anti-corrosion performance.

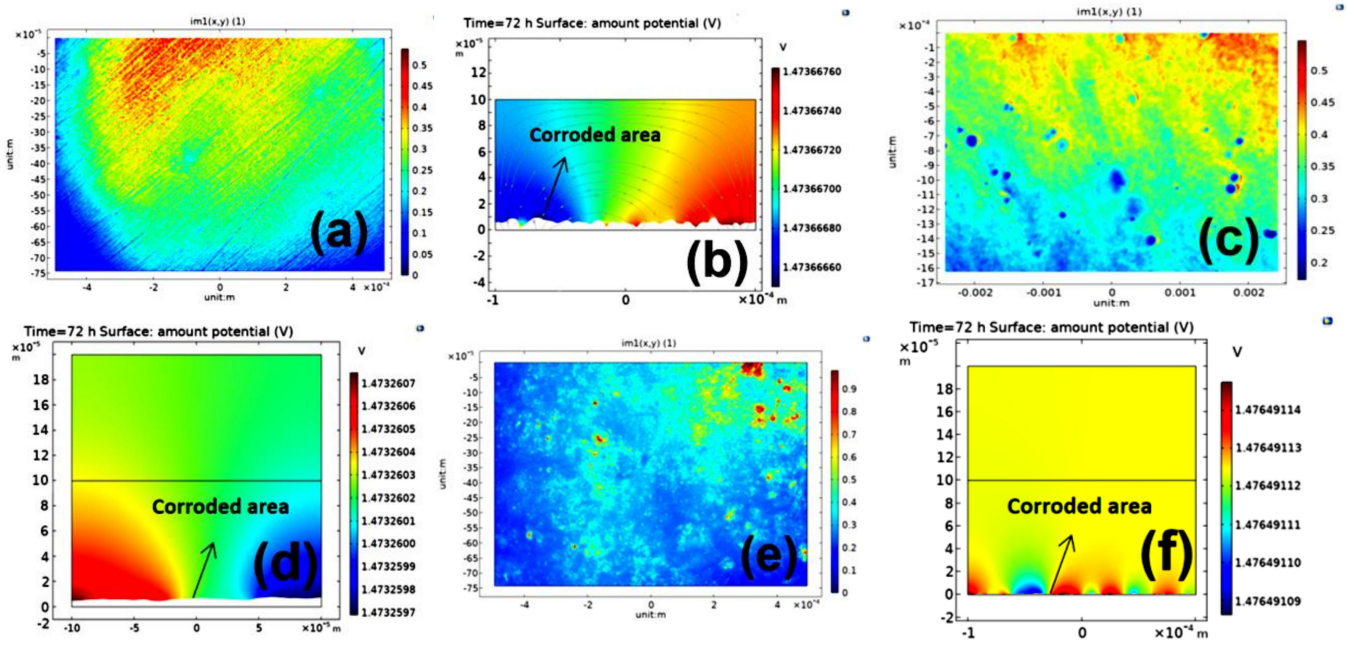

Figure 10. Finite element simulation of corrosion process by COMSOL software: (**a**) Modeling for specimen #1 by Figure 5a; (**b**) for specimen #1 after 72 h corrosion; (**c**) modeling for specimen #2 by Figure 5c; (**d**) for specimen #2 after 72 h corrosion; (**e**) modeling for specimen #3 by Figure 5e; (**f**) for specimen #3 after 72 h corrosion.

Figure 11 shows the results of the corrosion depth of the specimens simulated by COMSOL software. It can be seen from Figure 11a that the surface of specimen #1 is corroded rapidly during 72 h immersion, and the variation range of corrosion depth at different position is

0~2 × 10^{-5} m, which indicates that there is serious local corrosion. It can be seen from Figure 11b that the surface corrosion of specimen #2 is also serious during 72 h immersion, and the fluctuation range of corrosion depth at different positions is 5 × 10^{-6} m~8 × 10^{-6} m. Figure 11c shows that the corrosion depth of each position is near 7 × 10^{-7} m, indicating that the corrosion rate of the specimen #3 surface is the slowest. This demonstrates that the corrosion rate of metal substrate can be greatly reduced after superhydrophobic treatment. In addition, specimen #3 and specimen #2 are different only in the imported metallographic images during the simulation process, which further proves that the papillary bulges formed on the surface of specimen #3 play an important role in the improvement of its anti-corrosion performance, and also verifies the feasibility of this experimental method from a theoretical perspective.

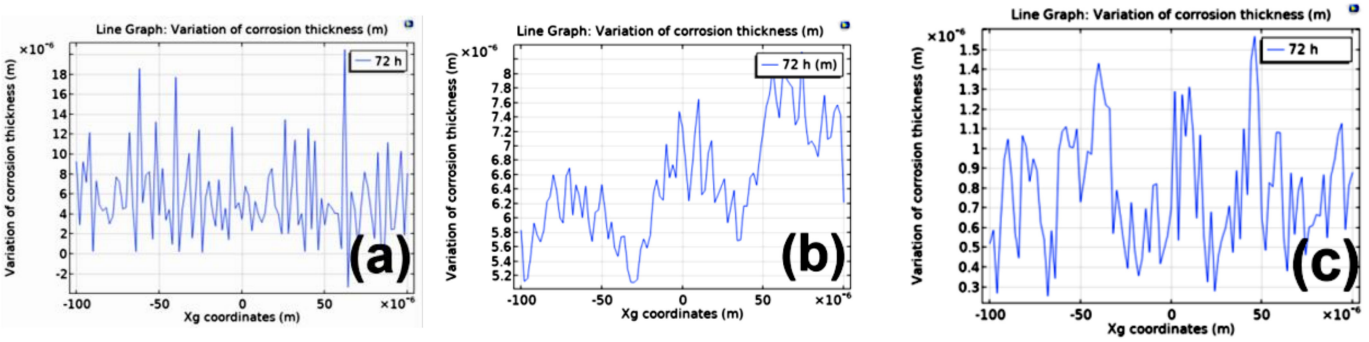

Figure 11. Corrosion thickness curves of COMSOL finite element simulation specimens after 72 h corrosion: (**a**) For specimen #1; (**b**) for specimen #2; (**c**) for specimen #3.

5. Conclusions

The surface of galvanized steel was treated by chemical etching method, and the surface was modified with a superhydrophobic treatment agent made of PFDTES and GO aqueous solution after varnish coating as specimen #3. Then, put specimen #3 into 3.0 wt% NaCl solution for the 72 h corrosion test together with specimen #1 (without surface treatment) and specimen #2 (only coated with varnish). The following conclusions are drawn from this research:

(1) The electrochemical test results indicate that the superhydrophobic coating of specimen #3 is beneficial to improve the impedance modulus of the metal surface and reduce the corrosion rate.
(2) Composition characterization shows that there is almost no corrosion product on the surface of specimen #3 after 72 h of immersion, while the other two specimens produce obvious corrosion products.
(3) The results of the surface topographies analysis show that specimen #3 has the best corrosion resistance compared with specimens #1 and #2, which may be related to the papillary bulges formed on the surface. COMSOL Multiphysics finite element simulation results, which are consisted with the results of experiment, also show function of the papillary bulges in anti-corrosion performance.
(4) The process of obtaining superhydrophobic coating is simple, without any high temperature treatment, and the experimental cycle is short. However, if applied to industrial production, the experimental process parameters need to be further optimized.

Author Contributions: Conceptualization, all the authors; methodology, W.C. and G.P.; investigation, H.S., W.C., W.L., A.Z., Y.Y., L.M.; writing—original draft preparation, W.C., H.S. and W.L.; writing—review and editing, W.C., H.S. and W.L.; software, W.L. and A.H. All authors have read and agreed to the published version of the manuscript.

Funding: The authors would like to acknowledge financial support from the School Enterprise Cooperation Project of Anhui Dingwang Environmental Protection Material Technology Co., Ltd. (W2020JSKF0565) and the Innovation and Entrepreneurship Training Program for College Students of Hefei University of Technology (S202210359338).

Data Availability Statement: All raw data supporting the conclusion of this paper are provided by the authors.

Acknowledgments: Thank you very much for the technical assistance of Cuiming Wu from the Analysis and Testing Center of Hefei University of Technology and the software support of the University of Science and Technology of China.

Conflicts of Interest: The authors declare no conflict of interest.

References

1. Bellini, C.; Cocco, D.C.; Lacoviello, F.; Mocanu, L.P. Impact of Copper, Tin and titanium addition on bending-induced damage of intermetallic phases in hot dip galvanizing. *Metals* **2022**, *12*, 2035. [CrossRef]
2. Rossi, S.; Pinamonti, M.; Calovi, M. Influence of Soil chemical characteristics on corrosion behaviour of galvanized steel. *Case Stud. Const. Mat.* **2022**, *17*, e01257. [CrossRef]
3. Kavunga, S.; Luckeneder, G.; Schachinger, E.D.; Faderl, J.; Fafilek, G. In situ characterization of galvanized low-alloyed steels with high-temperature cyclic voltammetry during annealing. *Electrochim. Acta.* **2022**, *424*, 140653. [CrossRef]
4. Duarte, T.; Meyer, Y.A.; Osório, W.R. The holes of Zn phosphate and hot dip galvanizing on electrochemical behaviors of multi-coatings on steel substrates. *Metals* **2022**, *12*, 863. [CrossRef]
5. Pang, K.; Hao, W.K.; Wu, J.S.; Peng, D.D.; Li, X.G. Corrosion behavior of field-exposed electrogalvanized steel plate in marine atmosphere. *Corros. Sci. Prot. Technol.* **2016**, *28*, 221–228.
6. Yin, R.H.; Zhang, L.; Dong, X.M.; Ji, X.B.; Zhang, X.S.; Cao, W.M.; Shi, X.H. Study on the formation of polyaniline coatings and its corrosion behavior from silane solutions. *Acta. Metall. Sin.* **2007**, *43*, 404–408.
7. Xiao, Y.D.; Li, X.L. Atmospheric corrosion of electroplated Zinc coatings. *Corros. Sci. Prot. Technol.* **1995**, *7*, 187–191.
8. Zhou, Y.; Huang, Z.; Liu, Y.; Chu, F. Comparative test on corrosion resistance of cold-sprayed Zinc and hot-dip galvanized steel for substation structure support. *Mech. Electr. Inf.* **2015**, *36*, 101–102.
9. Zhang, Q.S.; Gao, J.W.; Wang, C.Q.; Dai, G. Comparison of corrosion resistance of hot spray zinc, cold spray zinc and zinc rich coatings. *Corros.Technol.* **2017**, *38*, 903–913.
10. Xi, J.M.; Feng, L.; Jiang, L. A general approach for fabrication of superhydrophobic and superamphiphobic surfaces. *Appl. Phys. Lett.* **2008**, *92*, 53101. [CrossRef]
11. Cui, M.M.; Wang, B.; Wang, Z.K. Nature-inspired strategy for anticorrosion. *Adv. Eng. Mater.* **2019**, *21*, 1801379. [CrossRef]
12. Neinhuis, C.; Barthlott, W. Characterization and distribution of water-repellent, self-cleaning plant surfaces. *Ann. Bot.* **1997**, *79*, 667–677. [CrossRef]
13. Wang, S.; Liu, K.; Jiang, L.; Yao, X. Bioinspired surfaces with superwetability: New insight on theory, design, and applications. *Chem. Rev.* **2015**, *115*, 8230–8293. [CrossRef] [PubMed]
14. Sharma, V.; Kumar, S.; Reddy, K.L.; Bahuguna, A.; Krishnan, V. Bioinspired functional surfaces for technological applications. *J. Mol. Eng. Mater.* **2016**, *4*, 375–399. [CrossRef]
15. Zhang, C.; Liang, F.; Zhang, W.; Liu, H.; Tang, Y. Constructing mechanochemical durable and self-healing super-hydrophobic surfaces. *ACS Omega* **2020**, *5*, 986–994. [CrossRef] [PubMed]
16. Guo, X.G.; Li, X.M. An expanding horizon: Facile fabrication of highly superhydrophobic coatings. *Mater. Lett.* **2017**, *186*, 357–360. [CrossRef]
17. Tao, L.; Chen, S.; Cheng, S.; Tian, J.; Chang, X.; Yin, Y. Corrosion behavior of super-hydrophobic surfaces on copper in seawater. *Electrochim. Acta.* **2007**, *52*, 8003–8007.
18. Tu, K.; Wang, X.; Kong, L.; Guan, H. Facile preparation of mechanically durable, self-healing and multifunctional superhydrophobic surfaces on solid wood. *Mater. Design.* **2018**, *140*, 30–36. [CrossRef]
19. Weng, C.J.; Chang, C.H.; Lin, I.L.; Yeh, Y.M.; Wei, Y.; Hsu, C.L.; Chen, P.H. Advanced anticorrosion coating materials prepared from fluoro-polyaniline-silica composites with synergistic effect of superhydrophobicity and redox catalytic capability. *Surf. Coat. Technol.* **2012**, *207*, 42–49. [CrossRef]
20. Wang, H.; Fang, J.; Cheng, T.; Ding, J.; Qu, L.; Dai, L.; Wang, X.; Lin, T. One-step coating of fluoro-containing silica nanoparticles for universal generation of surface superhydrophobicity. *Chem. Commun.* **2008**, *7*, 877–879. [CrossRef]
21. Li, W.; Wang, H.; Li, Z. Preparation of golf ball-shaped microspheres with fluorinated polycaprolactone via single-solvent electrosprayingfor superhydrophobic coatings. *Prog. Org. Coat.* **2019**, *13*, 276–284. [CrossRef]
22. Li, Y.Q.; Si, W.T.; Gao, R.J. Facile preparation of superamphiphobic aluminum alloy surfaces and their corrosion resistance. *Surf. Coat. Technol.* **2022**, *430*, 127997. [CrossRef]
23. Haruna, K.; Saleh, T.A. Graphene oxide with dopamine functionalization as corrosion inhibitor against sweet corrosion of X60 carbon steel under static and hydrodynamic flow systems. *J. Electroanal. Chem.* **2022**, *920*, 116589. [CrossRef]

24. Mobin, M.; Huda Shoeb, M.; Aslam, R.; Banerjee, P. Synthesis, characterisation and corrosion inhibition assessment of a novel ionic liquid-graphene oxide nanohybrid. *J. Mol. Struct.* **2022**, *1262*, 13302. [CrossRef]
25. Cen, H.Y.; Chen, Z.Y. Amide functionalized graphene oxide as novel and effective corrosion inhibitor of carbon steel in CO2-saturated NaCl solution. *Colloid. Surf. A.* **2021**, *615*, 126216. [CrossRef]
26. Haruna, K.; Alhems, L.M.; Saleh, T.A. Graphene oxide grafted with dopamine as an efficient corrosion inhibitor for oil well acidizing environments. *Surf. Interfaces Anal.* **2021**, *24*, 101046. [CrossRef]
27. Ikhe., A.B.; Kale, A.B.; Jeong, J.; Reece, M.J.; Choi, S.-J.; Pyo, M. Perfluorinated polysiloxane hybridized with graphene oxide for corrosion inhibition of AZ31 magnesium alloy. *Corros. Sci.* **2016**, *109*, 238–245. [CrossRef]
28. Xie, Y.H.; Zhou, X.F.; Mi, H.Y.; Ma, J.H.; Yang, J.Y.; Cheng, J. High effificiency ZnO-based dye-sensitized solar cells with a 1H,1H,2H,2H-perflfluorodecyltriethoxysilane chain barrier for cutting on interfacial recombination. *Appl. Surf. Sci.* **2018**, *434*, 1144–1152. [CrossRef]
29. Chen, W.; Long, H.; Dong, J.; Wei, K.; Wen, H. Effect of pH value on the corrosion evolution of Q235B steel in simulated coastal-industrial atmospheres. *Acta Metall. Sin.* **2015**, *51*, 191.
30. Kamble, P.A.; Deshpande, P.P.; Vagge, S.T. Numerical investigation of galvanic corrosion between galvanized steel and mild steel in bolted joint. *Mater. Today Proc.* **2022**, *50*, 1923–1929. [CrossRef]
31. Harisha, D.V.N.; Bharatisha, A.; Narashima, H.M.; Anand, B.; Subramanya, K.N. Investigation of thermal residual stresses during laser ablation of tantalum carbide coated graphite substrates using micro-Raman spectroscopy and COMSOL multiphysics. *Ceram. Int.* **2021**, *47*, 3498–3513. [CrossRef]
32. Sawabe, T.; Akiyoshi, M.; Yoshida, K.; Yano, T. Estimation of neutron-irradiation-induced defect in 3C–SiC from change in XRD peak shift and DFT study. *J. Nucl. Mater.* **2011**, *417*, 430–434. [CrossRef]